





## Liquid metal convection induced by the Lorentz force in a Rayleigh-Bénard cell

Julien Guillou <sup>1,2</sup> Wladimir Bergez,<sup>1</sup> Rémi Zamansky <sup>1</sup> Anne Boulin <sup>2</sup>  
and Philippe Tordjeman <sup>1</sup>

<sup>1</sup>*Institut de Mécanique des Fluides de Toulouse (IMFT), Université de Toulouse-CNRS, 31400 Toulouse, France*

<sup>2</sup>*CEA, DEN/DET/SMTA/LMAG Cadarache, 13115 Saint-Paul-Lez-Durance, France*



(Received 9 February 2022; accepted 27 June 2022; published 15 July 2022)

We investigate by direct numerical simulation (DNS) the dynamics of a liquid metal in a cylindrical cell under the conjugate effects of a temperature gradient and an ac magnetic field. These numerical simulations are performed for a range of Hartmann and shielding parameters,  $30 \leq \text{Ha} \leq 301$  and  $1 \leq S_\omega \leq 68$ , which correspond to intermediate regimes between low and high frequency of the applied magnetic field. The scales of the physical parameters are discussed in order to analyze the DNS results. In our simulations, the Lorentz force overbalances the buoyancy force and is responsible for the flow patterns made of two tori. Each torus is characterized by a different average temperature which leads to different temperature gradients at the bottom and the top walls, and consequently different heat transfer to the outside. Thermal plumes advected between the two tori appear intermittently. The Lorentz force enhances the thermal exchanges even at a low Ha. We establish that a single master curve represents the evolution of the heat transfer characteristic of the different cases by plotting the  $\text{Nu}/\text{Pe}$  vs  $Q_J/Q_c$ , where Nu and Pe are the Nusselt and Péclet numbers, and  $Q_J$  and  $Q_c$  are the total power deposited by the Joule effect and the total power transferred without motion, respectively.

DOI: [10.1103/PhysRevFluids.7.073701](https://doi.org/10.1103/PhysRevFluids.7.073701)

### I. INTRODUCTION

The dynamics of conducting liquids under an electromagnetic field and a temperature gradient combines the effects of Rayleigh-Bénard convection (RBC), Joule heating, and Lorentz force. Such a situation is encountered in metallurgy [1,2] and liquid metal batteries [3], but also in the nuclear industry to simulate experimentally severe accidents [4]. The question of how the liquid dynamics govern the heat transfer is central in an academic context, but also to design technological systems.

For a given geometry characterized by the aspect ratio, the standard RBC is controlled by two dimensionless numbers, the Rayleigh number,  $\text{Ra} = \frac{g\beta\Delta T_0 L^3}{\alpha\nu}$ , and the Prandtl number,  $\text{Pr} = \frac{\nu}{\alpha}$ , where  $L$  and  $\Delta T_0$  are the characteristic length and the temperature difference;  $\nu$ ,  $\alpha$ , and  $\beta$  are the liquid viscous and thermal diffusion coefficients and the liquid thermal expansion coefficient, respectively; and  $g$  is the gravitational acceleration. Grossmann and Lohse [5] have established the existence of four turbulent flow regimes characterized by scaling laws of the Reynolds number  $\text{Re}$  and the Nusselt number  $\text{Nu}$ , as functions of  $\text{Ra}$  and  $\text{Pr}$ , based on the kinetic and thermal dissipation rates in the bulk and in the boundary layer. Here  $\text{Re}$  and  $\text{Nu}$  are defined as  $\text{Re} = \frac{UL}{\nu}$  and  $\text{Nu} = \frac{hL}{\kappa}$ , where  $U$  is the referenced velocity,  $h$  is the heat transfer coefficient, and  $\kappa$  is the thermal conductivity of the fluid. Typically, for metal liquids with  $\text{Pr} \sim 10^{-2}$  and  $\text{Ra} \sim 10^6$ ,  $\text{Re} \sim \text{Ra}^{1/2}\text{Pr}^{-3/4}$  and  $\text{Nu} \sim \text{Ra}^{1/4}\text{Pr}^{1/8}$ . However, the regimes are sensitive to the difference between the relative orientation of the temperature gradient and gravity acceleration [6,7].

A uniform heat generation in a fluid with no applied temperature difference between the top and the bottom of the cell induces fluid convection responsible for the temperature profile in the fluid. Under these conditions, the heat transfer is directly given by the maximum temperature difference and obeys to the same scaling law as in standard RBC ( $\text{Nu} \sim \text{Ra}^{1/4}$ ) [8,9]. These results are in agreement with the qualitative observations of Tritton and Zarraga [10]. For an infinite horizontal liquid layer, Xiang and Zikanov have shown that the condition for the onset of motion is significantly modified with respect to standard RBC, as three-dimensional (3D) convection cells are present at subcritical Rayleigh numbers [11]. To our knowledge, there are few studies on the fluid dynamics when a temperature gradient is superimposed to an internal heating. The linear stability analysis points out that the critical Rayleigh number decreases with the magnitude of the internal heating [12] and shows new destabilization hydrodynamics patterns resulting from the coupling between RBC and internal heating dynamics.

The stirring effects of an isothermal liquid metal by an alternating magnetic field depend on three dimensionless numbers, the magnetic Reynolds number,  $\text{Re}_m = \frac{UL}{\eta}$ ; the shielding parameter,  $S_\omega = 2\frac{L^2}{\delta^2}$ ; and the Hartmann number,  $\text{Ha} = B_0 L \sqrt{\frac{\sigma}{\rho\nu}}$ , where  $B_0$  is the magnitude of the magnetic field,  $\sigma$  and  $\rho$  are the electrical conductivity and mass density of the fluid,  $\eta$  is the magnetic diffusion coefficient, and  $\delta$  is the skin depth. It has been shown that for  $\text{Re}_m \ll 1$ , the kinetic energy of the fluid presents a maximum value for  $S_\omega \approx 20$  and decreases for higher  $S_\omega$  [13,14]. The Lorentz force, responsible for the flow, is distributed in the skin depth, which is a function of the ac pulsation  $\omega$ :  $\delta = \sqrt{\frac{2\eta}{\omega}}$ . Experiments show that the turbulent fluctuations are uniformly distributed in the bulk at low frequency. In contrast, they are mainly concentrated in the skin depth with a decrease of the integral scale at high frequency [14]. For  $\text{Re}_m \lesssim 20$  and a uniform external magnetic field, a quasilinear approximation of the magnetic diffusion equation can be used [15]. By accounting for the Hartmann layer thickness, the scaling relation of Grossmann and Lohse [5] for standard RBC has been extended to the magnetoconvection subject to a steady vertical magnetic field [16]. Recently, Akhmedagaev *et al.* [17] have simulated the fluid dynamics when the Lorentz force is coupled with RBC at a constant and uniform external magnetic field. They have found that for a high Hartmann number  $\text{Ha}$ , the flow pattern becomes quasi-two-dimensional with a structure reminiscent of vortex sheets. These structures are not observed at small  $\text{Ha}$ ,  $\text{Ha} \lesssim 50$ , and close to the marginal stability limit, for which three-dimensional patterns are persistent [18]. Under these conditions, the Lorentz force stabilizes the flow, and the turbulent fluctuations are damped.

Renaudière de Vaux *et al.* [19] have studied by direct numerical simulation (DNS) the destabilization of a liquid metal layer under the RBC conditions where an ac magnetic field produces heating by Joule effects (in this configuration, the Lorentz force has no effect). The DNS points out that the average kinetic energy of the fluid is independent of  $S_\omega$  and is a linear function of  $\text{Ra}$  based on a temperature scale defined by the Joule power heating. At low values of  $\text{Ra} \leq 10^5$ , the average temperature of the liquid varies as  $\text{Ra}^{-1/5}$ . A very recent numerical study in an axisymmetrical geometry investigates convection of metal heated by Joule effects in the presence of both Lorentz and buoyancy forces [20]. The authors found that the kinetic energy scales as  $\frac{\text{Ha}^2}{\text{Pr}_m}$ , where  $\text{Pr}_m = \frac{\nu}{\eta}$  is the magnetic Prandtl number. According to the dimensionless number definitions used by the authors, and considering the simulations are close to the marginal stability limit, we find again that the kinetic energy varies as  $\text{Ra}$ .

The literature analysis presented above is nonexhaustive, but clearly shows the difficulties in building a general understanding of the dynamics of liquid metal submitted to an ac magnetic field under RBC conditions. Indeed, the number of physical parameters, such as the geometry and the topology of the different fields (magnetic field, temperature gradient, acceleration of gravity, ...), is seldom the same from one study to another. Furthermore, this analysis reveals the importance of defining appropriately the relevant scales of the physical system. This point is critical for the definition of the temperature scale because it fixes  $\text{Ra}$  and the scaling laws between  $\text{Re}$  and  $\text{Nu}$  with this number.

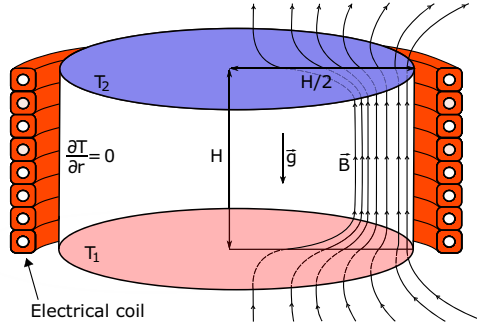


FIG. 1. Geometry of the Rayleigh-Bénard cell. Top and bottom wall temperatures are  $T_2$  and  $T_1$ , respectively, and the vertical wall is thermally insulated. The cell is filled with a liquid metal. The ratio of the gap between the coil and the liquid metal and the height is  $e/H = 0.15$ . The walls and the external medium are electrically nonconducting. The magnetic field is generated by an external electrical coil. As an example, magnetic field lines have been drawn at  $S_\omega = 15$ .

The general results can be summarized as follows.

- (i) In the RBC literature,  $Ra$  is simply calculated by the applied temperature difference. The dynamics are characterized by rolls at moderate  $Ra$ , and the average kinetic energy scales in  $Ra$ .
- (ii) When the fluid is heated internally by a uniform source, the flow patterns are similar to those of RBC for  $Ra$  defined by the maximum average temperature difference in the liquid.
- (iii) An external dc magnetic field has the main effect of mitigating the turbulent fluctuations, and it changes the flow pattern into quasi-two-dimensional structures at high  $Ha$ .
- (iv) With an ac external magnetic field, the kinetic energy of the fluid reaches a maximum value when  $S_\omega$  is increased with a stirring effect inside the bath.
- (v) When the effect of the Lorentz force is negligible and the temperature scale is defined by internal heat generation by the Joule effect, the average kinetic energy scales again as  $Ra$ .
- (vi) Finally, there are very few studies on the heat transfer when RBC, Joule heating, and Lorentz force control the flow dynamics.

This paper aims to study the magnetoconvection of a liquid metal in a vertical cylinder. In this paper, we study by numerical simulations the dynamics of the liquid metal when an ac magnetic field and a temperature difference are applied to the cylinder. In such a situation, the velocity and temperature fields result from the coupling, on the one hand, of the Lorentz and the buoyancy forces and, on the other hand, of the Joule effect and the temperature gradient. The simulations are realized under the interesting conditions where the Lorentz force is dominating while the Joule effect and the temperature gradient both contribute weakly to the global dynamics and heat transfer. With these conditions, we find that the heat transfer is at first order controlled by forced convection with intermittent perturbations due to buoyancy. The paper is organized as follows. In Sec. II, the system is described and the equations for the flow and the heat transfer are presented. An important discussion on the scales of the system is also given in this section. The numerical simulations are introduced in Sec. III, and the results are discussed in Sec. IV.

## II. PHYSICS OF THE STUDIED SYSTEM

We consider a vertical cylinder of aspect ratio  $H/D = 1$ , where  $H$  and  $D$  are its height and diameter (see Fig. 1), filled with a liquid metal ( $Pr = 2.98 \times 10^{-2}$ ,  $Pr_m = 1.35 \times 10^{-6}$ ). The top and the bottom walls are supposed to remain at constant temperatures, respectively,  $T_2$  and  $T_1$ . The temperature difference  $\Delta T_0 = T_1 - T_2$  is fixed in this study and the Rayleigh number based on this scale is  $Ra = 3.86 \times 10^6$ , larger than the critical value characteristic of RBC ( $Ra_c = 2261.86$  [21]). The vertical wall is assumed to be a perfect electrical and thermal insulator, and the no-slip condition

TABLE I. Values of the parameters  $B_0$ ,  $S_\omega$ , Ha, Re,  $\text{Re}_m$ , and Ra of the DNS for three different values of  $I_0$  and six frequencies  $f$ .

$I_0$ (A)	10						50						100					
$f$ (Hz)	15	150	300	500	750	1000	15	150	300	500	750	1000	15	150	300	500	750	1000
$B_0 \times 10^3$ (T)	7.16						35.81						71.63					
$S_\omega$	1	10	15	20	34	68	1	10	15	20	34	68	1	10	15	20	34	68
Ha	30						151						301					
$\text{Re} \times 10^{-3}$	5.02	6.07	5.41	6.05	5.64	5.41	7.18	33.10	29.65	29.74	28.80	27.69	15.6	78.02	70.71	69.32	66.59	66.90
$\text{Re}_m \times 10^2$	0.67	0.82	0.73	0.82	0.76	0.73	0.97	4.46	4.00	4.00	3.88	3.73	2.11	10.52	9.53	9.34	8.98	9.02
$\text{Ra} \times 10^{-6}$							3.86											

at all boundaries is imposed for the fluid velocity  $\mathbf{u}$ . An axisymmetric ac magnetic field,  $\mathbf{B}(\mathbf{r}, t)$ , is generated by an electrical current,  $I_0$ , through a coil positioned around the cylinder. The two control parameters are  $S_\omega$  and Ha and vary in the ranges  $1 \leq S_\omega \leq 68$  and  $30 \leq \text{Ha} \leq 301$  (Table I). We have also considered the reference case  $\mathbf{B} = \mathbf{0}$  (Ha = 0) corresponding to standard RBC.

The magnetic induction in a liquid metal results from the time variation of  $\mathbf{B}(\mathbf{r}, t)$  and the velocity of the liquid. The magnetic field in the liquid can be expressed as the sum of the magnetic field in the absence of motion,  $\mathbf{B}_0(\mathbf{r}, t)$ , and the perturbation due to the velocity field,  $\mathbf{b}(\mathbf{r}, t)$ . The induction equation for  $\mathbf{b}(\mathbf{r}, t)$  is then

$$\partial_t \mathbf{b} = \eta \nabla^2 \mathbf{b} + \nabla \times (\mathbf{u} \times \mathbf{b}) + \nabla \times (\mathbf{u} \times \mathbf{B}_0). \quad (1)$$

The ratio of the magnitude of the first and second terms on the right-hand side of this equation is the magnetic Reynolds number,  $\text{Re}_m$ . The nonlinear term of Eq. (1) is, therefore, negligible when  $\text{Re}_m \ll 1$ .

At small frequency, i.e.,  $S_\omega \sim 1$ , and  $\text{Re}_m \ll 1$ , Eq. (1) yields the quasistatic diffusion equation, which implies  $\frac{b_0}{B_0} \sim O(\text{Re}_m)$ , where  $b_0$  is the scale of the perturbation field. This result has been confirmed in Ref. [15] for a dc magnetic field up to  $\text{Re}_m = 1$ . At high frequency, i.e.,  $S_\omega \sim 100$ , the quasistatic assumption is not valid, and the natural length scale is  $\delta$ , the penetration depth of  $\mathbf{B}_0(\mathbf{r}, t)$ . Under this condition, the three linear terms in Eq. (1) are of the same order of magnitude, and  $\frac{b_0}{B_0} \sim O(\frac{\text{Re}_m}{\sqrt{S_\omega}})$ . Moreover, the perturbation terms in the Lorentz force can be neglected if  $\text{Re}_m \ll 1$  and  $\frac{\sqrt{2S_\omega}}{\text{Re}_m} \gg 1$  (see the Appendix). In this case, it is not necessary to solve  $\mathbf{b}(\mathbf{r}, t)$ . These conditions on  $\text{Re}_m$  and  $S_\omega$  are verified in all our DNSs (Table I). We have assumed that the magnetic field in the liquid metal is then given by the static case,  $\mathbf{B}(\mathbf{r}, t) = \mathbf{B}_0(\mathbf{r}, t)$ , and the Lorentz force is  $\mathbf{F}_L = \frac{1}{\mu_0} (\mathbf{B}_0 \cdot \nabla \mathbf{B}_0 - \nabla \frac{B_0^2}{2})$ . Assuming the liquid metal is incompressible, the second term contributes only to the hydrostatic pressure.

The magnetic and electrical fields,  $\mathbf{B}_0$  and  $\mathbf{E}_0$ , applied to the liquid metal are the solution of the following set of equations:

$$\nabla \cdot \mathbf{B}_0 = 0, \quad (2a)$$

$$\partial_t \mathbf{B}_0 = -\nabla \times \mathbf{E}_0, \quad (2b)$$

$$\nabla \times \mathbf{B}_0 = \mu_0 [\mathbf{J}_0 + \mathbf{J}^e(t)], \quad (2c)$$

$$\mathbf{J}_0 = \sigma \mathbf{E}_0, \quad (2d)$$

where  $\mathbf{J}_0$  and  $\mathbf{J}^e(t)$  are the current density vectors in the liquid metal and in the coil, respectively. Solving for  $\mathbf{B}_0$ , the Lorentz force can be computed for different values of  $I_0$  and  $S_\omega$ . As an example, the left part of Fig. 2 presents the spatial distribution of the norm of the first term of  $\mathbf{F}_L$  for  $S_\omega = 10$

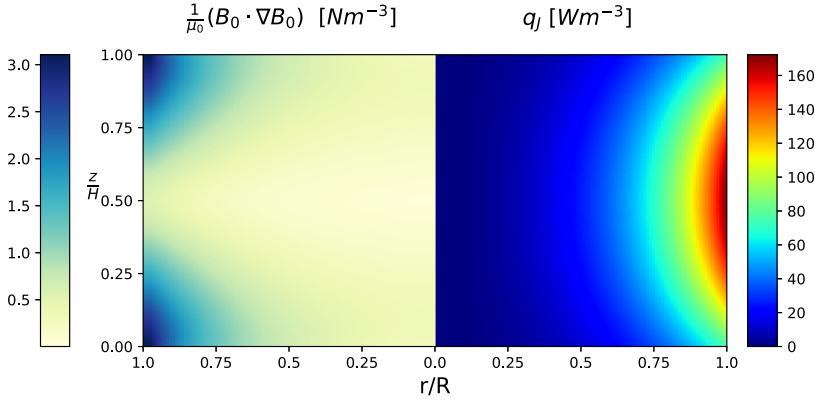


FIG. 2. Distribution of  $|\frac{1}{\mu_0} \mathbf{B}_0 \cdot \nabla \mathbf{B}_0|$  responsible for the fluid motion (left part of the cell cross section) and  $q_J$  (right part) for  $I_0 = 1$  A and  $S_\omega = 15$ .

and  $I_0 = 1$  A. This figure shows that the force is localized at the two corners, top and bottom, of the cylinder. The right part of Fig. 2 presents the power density  $q_J = \frac{J_0^2}{\sigma} = \frac{\eta}{\mu_0} (\nabla \times \mathbf{B}_0)^2$  due to the Joule effect at  $S_\omega = 10$ , which is localized in the skin depth close to the vertical wall. The details of the computation of the field  $\mathbf{B}_0$ , used to compute both the Lorentz force and the Joule heating, are given in the next section.

The total power deposited by the Joule effect in the liquid metal,  $Q_J = \int q_J dV$ , normalized by the heat transferred by pure conduction,  $Q_c = k \Delta T_0 \frac{\pi D^2}{4H}$ , is plotted as a function of  $S_\omega$  [Fig. 3(a)]. This curve shows that there are two asymptotic behaviors: the power scales as  $S_\omega^2$  for  $S_\omega < 1$  and  $\sqrt{S_\omega}$  for  $S_\omega > 100$ . In parallel, the spatially averaged amplitude of the Lorentz force, normalized by the buoyancy force,  $F_B = \rho g \beta \Delta T_0 \frac{\pi}{4} D^2 H$ , scales as  $S_\omega$ , for  $S_\omega < 1$ , and is constant for  $S_\omega > 100$ . We find that these scaling relations are the same as in the case of an infinite cylinder. In this work, all the simulations are realized in the intermediate region, i.e.,  $1 < S_\omega < 100$ .

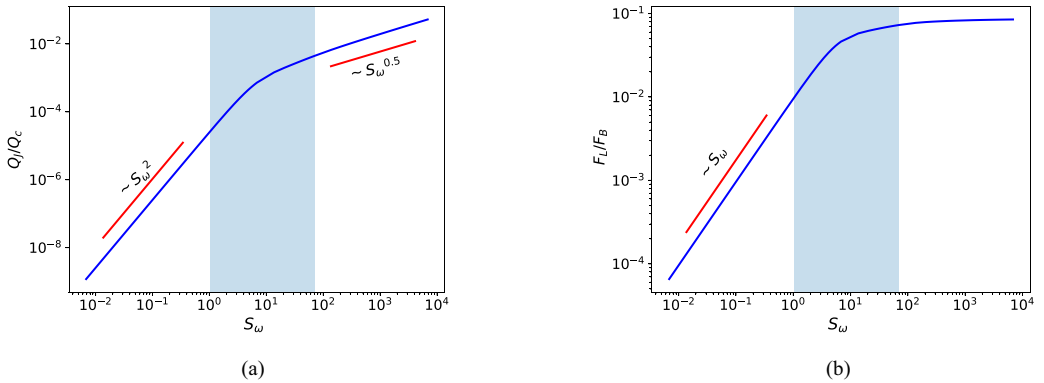


FIG. 3. (a) Joule heating total power  $Q_J$  in the liquid metal volume normalized by  $Q_c$  versus the shielding parameter  $S_\omega$ . (b) Volume-average Lorentz force normalized by  $F_B$  versus the shielding parameter  $S_\omega$ . Each curve is computed at  $I_0 = 1$  A; the power laws in  $S_\omega$  are mentioned on each curve. The colored domain indicates the range of variation of  $S_\omega$  for the DNS.

The motion of the liquid metal is governed by the Oberbeck-Boussinesq equations, including the additional Lorentz force and Joule heating:

$$\frac{\partial \mathbf{u}}{\partial t} + \mathbf{u} \nabla \mathbf{u} = -\frac{1}{\rho} \nabla P + \nu \Delta \mathbf{u} + \beta T \mathbf{g} + \frac{1}{\rho \mu_0} \mathbf{B}_0 \cdot \nabla \mathbf{B}_0, \quad (3a)$$

$$\frac{\partial T}{\partial t} + \mathbf{u} \cdot \nabla T = \alpha \Delta T + \frac{\mathbf{J}_0^2}{\rho c_p \sigma}, \quad (3b)$$

$$\nabla \cdot \mathbf{u} = 0. \quad (3c)$$

In the momentum equation (3a),  $P$  is the total pressure including the magnetic pressure. In addition, the two forces responsible for the flow are the buoyancy force and the Lorentz force.  $T$  is the temperature relative to the top temperature  $T_2$ , and  $c_p$  is the specific heat of the liquid metal. For the heat equation (3b), the two source terms are  $\Delta T_0$  imposed at the boundaries and the Joule heating in the volume. We recall that the boundary conditions are a no-slip condition on the walls for the velocity, Dirichlet conditions on top and bottom walls for the temperature with the difference amplitude  $\Delta T_0$ , and an adiabatic condition on the vertical wall.

To obtain dimensionless equations, it is necessary to define the characteristic scales of the simulated system. We can define two velocity scales from the buoyancy force and the Lorentz force,  $U_B = \sqrt{g\beta\Delta T H}$  and  $U_L = B_0/\sqrt{\mu_0\rho}$ , respectively.  $U_L$  is also known as the Alfvén velocity. The temperature scale  $\Delta T$  is either  $\Delta T_0$  or  $\Delta T_L$ , the characteristic temperature difference due to the Joule effect obtained by an energy balance:

$$\Delta T_L = \frac{\langle q_J \rangle H}{\rho c_p U}, \quad (4)$$

where  $\langle q_J \rangle$  is the volume average of the power density amplitude, and  $U$  is the reference velocity  $U_B$  or  $U_L$ . Depending on the choice of  $U$ , two definitions of  $\Delta T_L$  follow with different scalings at high and low frequencies:

- (i) for  $U = U_B$ :  $\Delta T_L \sim S_\omega^2 Ha^2$  at  $S_\omega < 1$ , and  $\Delta T_L \sim S_\omega Ha^2$  at  $S_\omega > 1$ ;
- (ii) for  $U = U_L$ :  $\Delta T_L \sim S_\omega^2 Ha$  at  $S_\omega < 1$ , and  $\Delta T_L \sim S_\omega Ha$  at  $S_\omega > 1$ .

Four regimes appear when  $U_L/U_B$  is plotted versus  $\Delta T_L/\Delta T_0$ :

- (i)  $\Delta T_L < \Delta T_0$  and  $U_L < U_B$ : dynamics is piloted by the buoyancy force giving a RBC flow pattern;
- (ii)  $\Delta T_L > \Delta T_0$  and  $U_L < U_B$ : dynamics is controlled by the buoyancy force and the volume heating by the Joule effect;
- (iii)  $\Delta T_L < \Delta T_0$  and  $U_L > U_B$ : the Lorentz force governs the dynamics, but the heat transfer is due to the imposed temperature difference  $\Delta T_0$ ;
- (iv)  $\Delta T_L > \Delta T_0$  and  $U_L > U_B$ : the Lorentz force and the heating by the Joule effect dominate.

Figure 4 shows that our numerical simulations are realized in a regime where the Lorentz force is prominent and the heat transfer is controlled by the wall temperature difference  $\Delta T_0$ . Hence, the interest of these simulations is to study the dynamics of the liquid metal under forced convection by the Lorentz force, perturbed by the Joule heating and the buoyancy force.

Based on the previous scales ( $H$  for length,  $\Delta T_0$  for temperature,  $U_L$  for velocity,  $H/U_L$  for time,  $\rho U_L^2/2$  for pressure,  $B_0 = \mu_0 n I_0/H$  for magnetic field, where  $n$  is the number of turns of the coil,  $\sigma \omega H B_0$  and  $\sigma \omega \delta B_0$  at low and large frequencies, respectively, for the electrical current density), one can write the dimensionless physical equations of our problem:

$$\frac{\partial \mathbf{u}}{\partial t} + \mathbf{u} \nabla \mathbf{u} = -\nabla P + \frac{\sqrt{\text{Pr}_m}}{\text{Ha}} \Delta \mathbf{u} + \frac{\text{RaPr}_m}{\text{PrHa}^2} T \cdot \mathbf{e}_z + S_\omega^k \mathbf{B}_0 \cdot \nabla \mathbf{B}_0, \quad (5a)$$

$$\frac{\partial T}{\partial t} + \mathbf{u} \nabla T = \frac{\sqrt{\text{Pr}_m}}{\text{HaPr}} \Delta T + S_\omega^{2k} \text{Ha} \sqrt{\text{Pr}_m} \Gamma \mathbf{J}_0^2, \quad (5b)$$

$$\nabla \cdot \mathbf{u} = 0. \quad (5c)$$

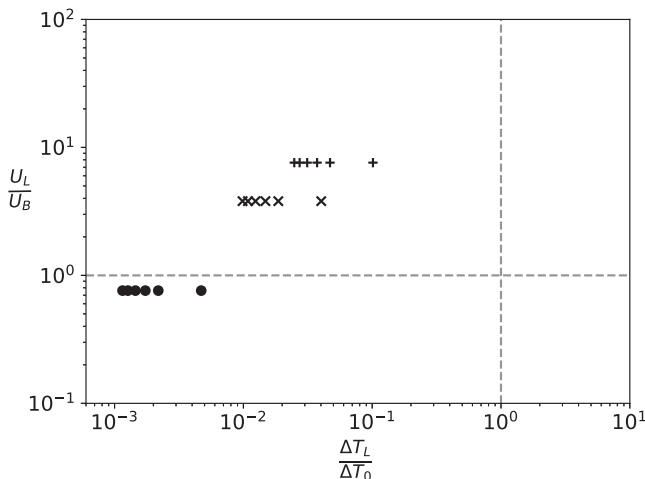


FIG. 4. Map of the regimes of the magnetoconvection in the Rayleigh-Bénard cell. Symbols correspond to DNS:  $I_0 = 10$  A ( $\bullet$ ), 50 A ( $\times$ ), and 100 A ( $+$ ).

In these equations, the buoyancy force per unit volume varies as  $\frac{\text{RaPr}_m}{\text{Ha}^2\text{Pr}}$ . One notes that the magnitude of the Joule heating source term is  $\Gamma\text{Ha}\sqrt{\text{Pr}_m}S_\omega$  and  $F_L \sim \sqrt{S_\omega}$  for  $S_\omega > 10$  ( $k = 1/2$ ), and  $\Gamma\text{Ha}\sqrt{\text{Pr}_m}S_\omega^2$  and  $F_L \sim S_\omega$  for  $S_\omega < 10$  ( $k = 1$ ), where  $\Gamma = \frac{\eta^3}{c_p\Delta T_0 H^2}$ . For all the numerical simulations,  $\Gamma$  is fixed and equal to  $1.4 \times 10^{-3}$ .

### III. NUMERICAL SIMULATIONS

For the simulations, we consider a cylinder filled with a liquid metal (Galinstan) and submitted to a temperature difference of 10 K (top and the bottom temperatures are 293 and 303 K, respectively). The magnetic field within the cell is computed with COMSOL for the different values of current intensity and frequency listed in Table I. The Maxwell equations (2) have been solved in 2D axisymmetric geometry for  $H = D = 0.1$  m and a coil of rectangular section  $5 \times 5$  mm<sup>2</sup> having 19 turns and 3 layers. The gap between the coil and the liquid metal is 15 mm. The results for a structured grid  $N_r \times N_z = 512 \times 1024$  have been compared and validated with MAXWELL ANSYS.

The liquid metal has the following properties:  $\rho = 6300$  kg m<sup>-3</sup>,  $\sigma = 3.46 \times 10^6$  S m,  $\nu = 3.10 \times 10^{-7}$  m<sup>2</sup> s<sup>-1</sup>,  $\beta = 1.27 \times 10^{-4}$  K<sup>-1</sup>,  $\alpha = 1.08 \times 10^{-5}$  m<sup>2</sup> s<sup>-1</sup>, and  $c_p = 370$  J kg<sup>-1</sup> K<sup>-1</sup>. Values of  $S_\omega$  and Ha are summarized in Table I. As an illustration, the magnetic field lines are displayed in Fig. 1 for  $S_\omega = 15$ . Equations (5) are solved with the finite volume code JADIM. This code uses a third-order Runge-Kutta scheme for temporal integration. The spatial derivatives are calculated with second-order accuracy. Incompressibility is achieved through a projection method. The viscous terms are calculated using a semi-implicit Crank-Nicolson scheme. The description of the numerical methods used in the computations can be found in Ref. [22]. The 3D mesh in cylindrical coordinates is chosen in order to respect the DNS criteria of Grötzbach [23]. The grid is composed of  $N_r \times N_\theta \times N_z = 128 \times 256 \times 256$  points. The magnetic field computed with COMSOL with a resolution much finer than the DNS grid, is sampled at the vertices of the DNS grid. The COMSOL simulations provide the magnitude and phase of the magnetic field inside the liquid. Consequently, the magnetic field can be computed at each instant in the DNS simulations. Using Amperes' law to calculate the eddy current density, the Joule heating and the Lorentz force are directly calculated in JADIM. More details of the calculation process are presented in Ref. [24]. For comparison purpose, we have performed a RBC DNS with different Ra between  $3.86 \times 10^5$  and  $3.86 \times 10^6$ . The results are in good agreement with the scaling law predicted by Grossman and Lohse [5]. Additionally,

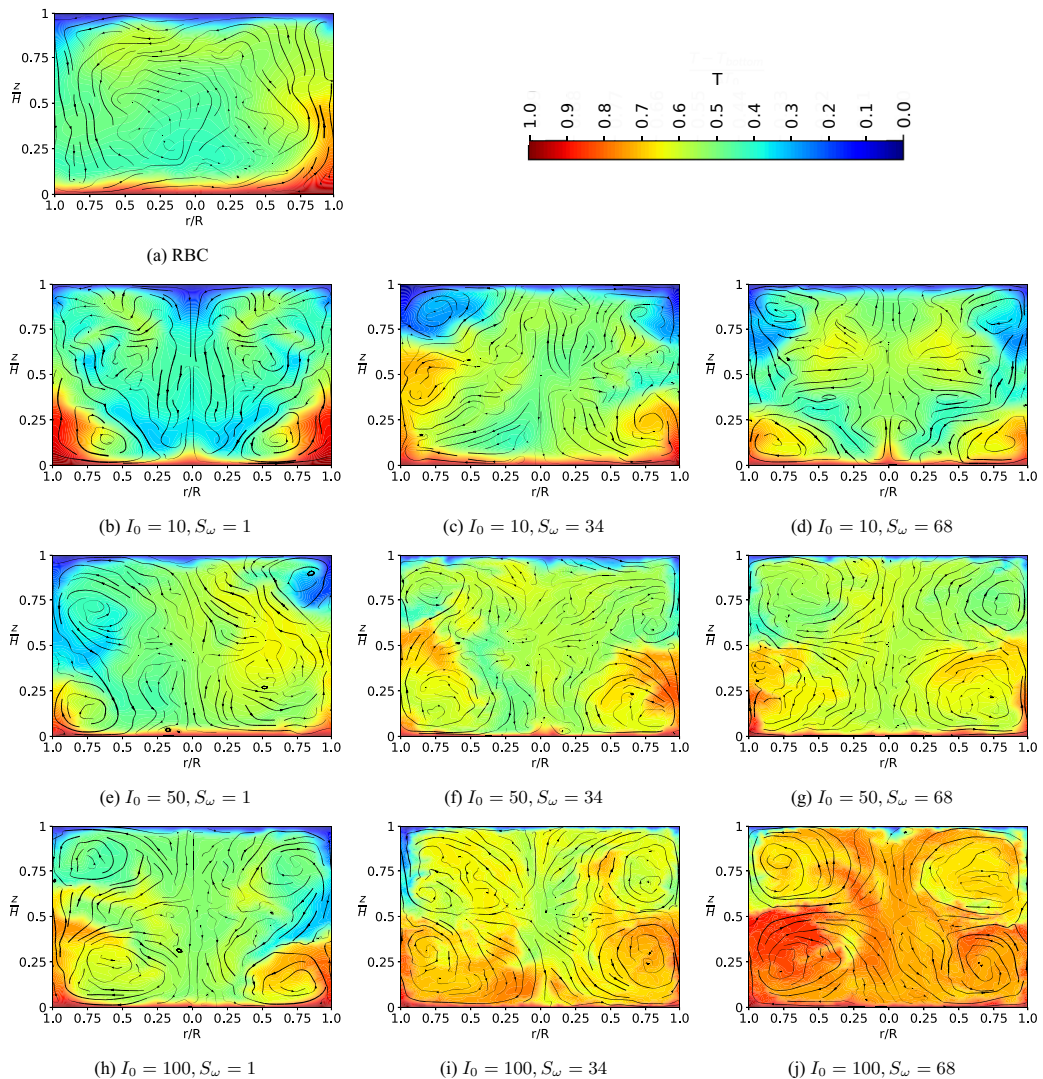


FIG. 5. Instantaneous snapshots in a vertical cross section of the temperature and of the flow streamlines computed by DNS. Panel (a) represents the RBC reference case. Panels (b)–(d) correspond to  $I_0 = 10$  A and  $S_\omega = 1, 34$ , and  $68$ ; panels (e)–(g) correspond to  $I_0 = 50$  A and  $S_\omega = 1, 34$ , and  $68$ ; and panels (h)–(j) correspond to  $I_0 = 100$  A and  $S_\omega = 1, 34$ , and  $68$ .

we have solved the heat equation with a solid conductor submitted to Joule heating in the same geometry for all the conditions of frequency and current intensity, in order to compare our DNS to this reference case. All the results presented below correspond to statistically stationary regimes and the velocity and temperature data are averaged in time. As specified below, when appropriate, we also sometimes consider spatial averaging.

#### IV. RESULTS AND DISCUSSION

Figure 5 displays the instantaneous streamlines and temperature snapshots of the RBC reference case ( $Ha = 0$ ) and for three current intensities and three frequencies (see Table I). The snapshot



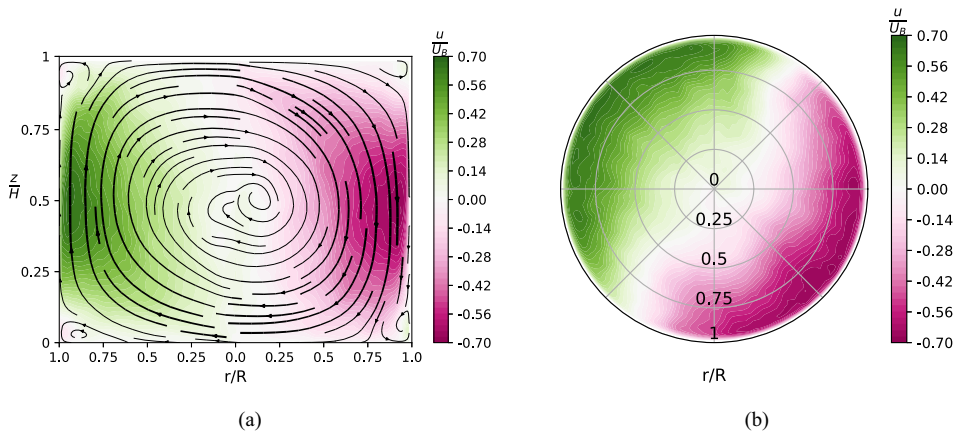


FIG. 6. RBC reference case. (a) Time average of the vertical velocity  $u/U_B$  in a cross section plotted with the velocity streamlines. (b) Distribution of the vertical velocity in the midplane.

of RBC, observed in Fig. 5(a) shows that the temperature distribution, in the boundary layer, is correlated with the velocity streamlines, with hot and cold regions tending to move upwards and downward, respectively. In the bulk of the flow, we observe that the temperature is quite uniform. Compared to RBC, the Lorentz force strongly modifies the patterns. Indeed, the unique convection cell in RBC is changed to two toroidal cells in forced convection at 50 and 100 A. The patterns at 10 A exhibit an intermediate regime when the Lorentz force balances the buoyancy force. The variation of the temperature field shows clearly a transition in the convective heat transfer process when the current intensity is applied. It is seen that the temperature distribution also follows the velocity streamlines, confirming the overall importance of advection phenomena in this flow. Moreover, the two tori appear to be at different temperatures, high temperature for the lower torus and low temperature for the upper one. In the presence of the magnetic field, the temperature distribution tends to be axisymmetric, whereas this symmetry is broken in RBC.

Concerning the RBC reference case, the average velocity fields show the well-known large-scale circulation (Fig. 6). In this case, the characteristic velocity is given by the buoyancy and the imposed temperature difference  $\Delta T_0$ . The flow pattern is then a unique convection cell where the liquid goes up on one side of the cell and goes down on the other side. Consequently, the axial symmetry is broken as mentioned above. For a very large timescale, the convection cell turns around the cylinder axis with the dynamics characterized by a precession period much larger than the advection time  $\frac{H^2}{\nu Re}$  [25]. Note that we also compute the Rayleigh and Nusselt numbers and find a very good agreement with the literature [26].

When imposing an alternating magnetic field, the average flow patterns are drastically modified. They present two toroidal cells, for all current intensities and frequencies considered in this study. Figure 7 presents the average vertical velocity for  $Ha = 301$  and  $S_\omega = 34$  in horizontal and vertical planes of the cell. These patterns are characterized by two rectangular tori positioned one over the other with an opposite azimuthal vorticity. The revolution axis of the two tori coincides with the axis of the cell cylinder [Fig. 7(a)]. For  $z < H/2$  the liquid metal goes upward close to the wall and goes downward in the bulk. Conversely, for  $z > H/2$  the liquid turns in the opposite direction and goes down along the wall and upward in the center of the cell. Hence, the maximum mean azimuthal vorticity is localized at  $r \approx 0.75R$ . Figure 7(b) displays the vertical velocity profile averaged in time and in azimuth angle for various  $r$  in the function of the vertical position. The S curve presents two extrema at the center of the tori at  $z \approx 0.25H$  and  $z \approx 0.75H$ . In the midplane of the cell ( $z = 0.5$ ), the vertical mean velocity is almost zero for all  $r$ . Figures 7(c) and 7(d) compare the vertical average velocity distributions at  $z = 0.25$  and  $z = 0.75$ . These two figures show that the distribution of the

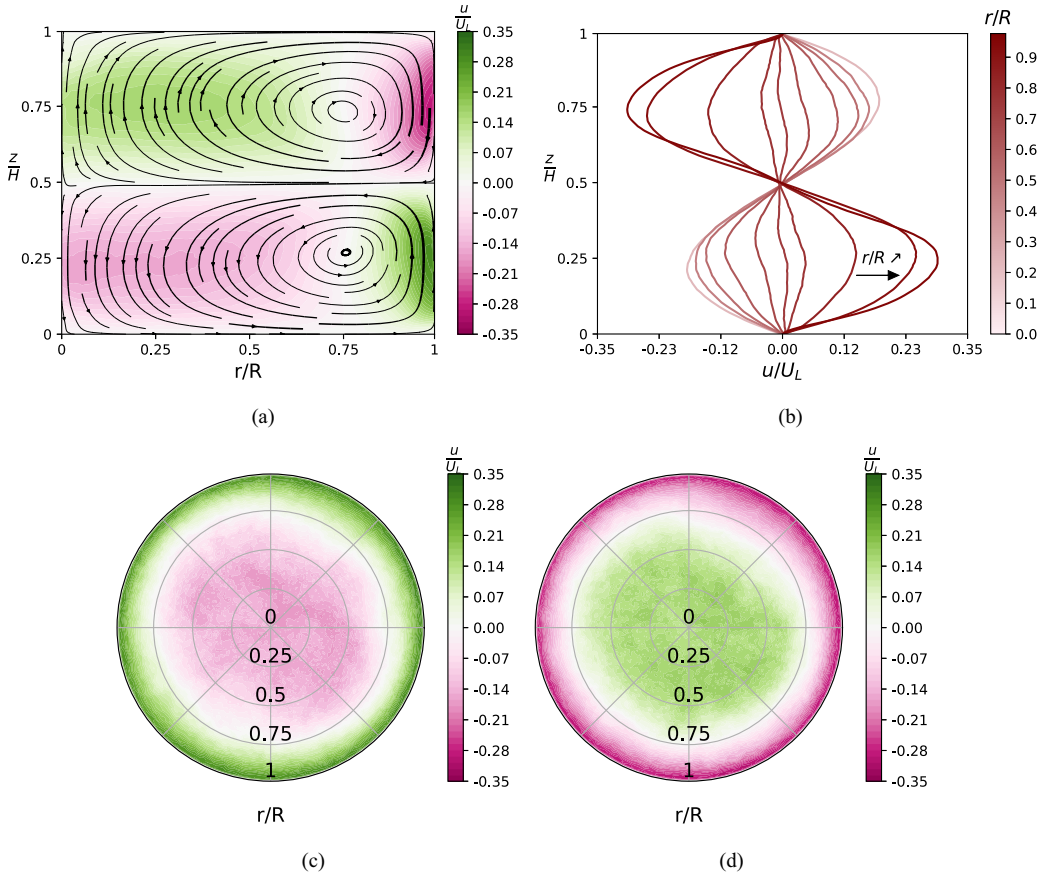


FIG. 7. Distribution of the average vertical velocity at  $I_0 = 100$  A and  $S_\omega = 34$  computed by DNS. (a) Torus streamlines in vertical cross section of the time and azimuth averaged velocity. (b) Vertical profiles for various radial positions. (c) and (d) Distribution of the vertical velocity at  $z = 0.25$  and  $z = 0.75$ .

vertical velocity is approximately axisymmetric. Moreover, the vertical velocity is antisymmetric, with respect to the midplane, as also observed in Fig. 7(b).

This double-torus flow structure is still observed for all the lower values of the current intensity [24]. The DNS show smooth transition between the RBC patterns and the toroidal pattern when  $I_0$  increases. At 10 A, the flow is characterized by a mixture between free convection and forced convection. The torus appears and disappears alternatively. At 50 and 100 A, the toroidal patterns are well established with the same trend of stabilization with frequency. This typical evolution of the flow patterns can be observed in Fig. 5. Hence, the RBC pattern is still reminiscent at low current intensity and frequency. The structure of this convection cell disappears when the frequency increases. Consequently, in our simulations, the Lorentz force is responsible for the two-tori flow pattern. The videos presented in Ref. [24] show clearly these main features.

Figure 8 presents the root-mean-square (rms) velocity computed over the whole volume as a function of  $S_\omega$  for the three Ha values. These curves show that the maximum fluctuation intensity is reached at  $S_\omega \approx 10$  in agreement with Ref. [13]. For  $S_\omega > 10$ , the rms velocity decreases slightly, which can be related to a constant Lorentz force [Fig. 3(b)]. The rms is then on the order of  $U_L/10$ . In Table I, we present as well the values of the Reynolds number based on this rms velocity, which show similar trends.

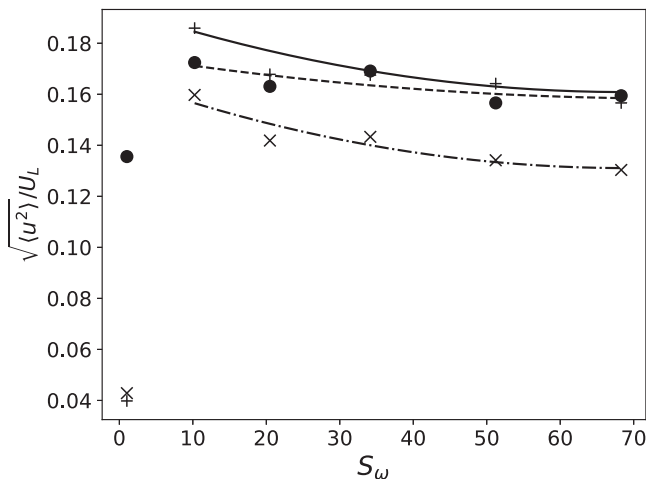


FIG. 8. Root mean square of the time-averaged vertical velocity  $\sqrt{\langle u^2 \rangle}/U_L$  vs  $S_\omega$ . Symbols:  $I_0 = 10$  A ( $\bullet$ ), 50 A ( $\times$ ), and 100 A ( $+$ ). The lines give the tendency.

As the mean vertical velocity is zero in the midplane, the mass transfer and the heat transfer between both tori, and thus between the two horizontal walls, are controlled by fluctuations of the velocity field. In this region, the flow presents on average the structure of a plane jet pointed radially inward, subject to the mean vertical temperature gradient. In the snapshots of Fig. 5, we observe thermal plumes going up [Figs. 5(e), 5(f), and 5(i)] or down [Fig. 5(h)] originated from the midplane close to the walls. The videos of simulations show clearly the dynamics of these plumes, which appear intermittently without breaking the torus configuration [24]. The signature of the thermal plumes is visible in the map of the vertical velocity variance shown in Fig. 9 for  $Ha = 150$  and  $S_\omega = 10$ . This figure points out that the velocity fluctuations are maximum in the midplane and close to the wall, where the Joule heating is the largest. In this region, the characteristic value of the rms is of the order of  $U_L/10$  as already reported for the global characteristic velocity. We mentioned that the normalized variance map remains similar whatever the  $Ha$  value, at high frequency ( $S_\omega \geq 10$ ) [24].

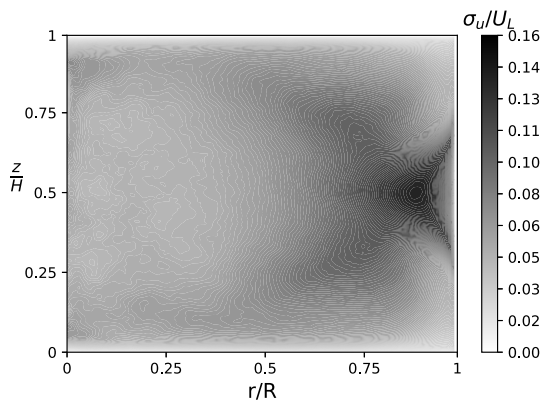


FIG. 9. Dimensionless standard deviation of the vertical velocity in a vertical cross section for  $I_0 = 50$  A and  $S_\omega = 10$ , obtained from time and azimuthal averaging.

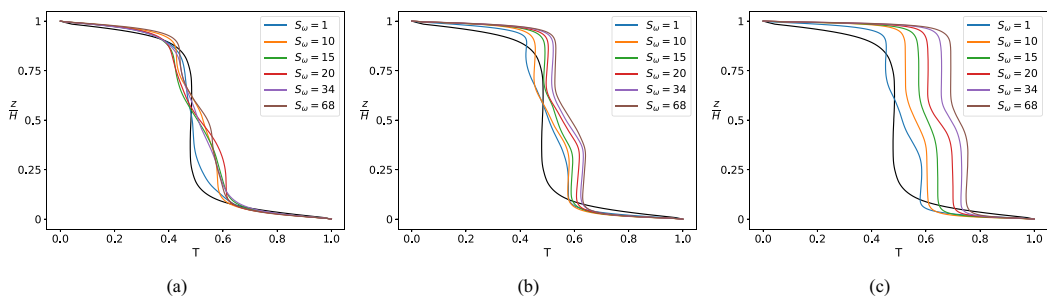


FIG. 10. Horizontal average of the dimensionless liquid temperature for different values of  $S_\omega$  at  $I_0 = 10$  A (a), 50 A (b), and 100 A (c). The black curves display the temperature profile of the RBC reference case.

Qualitatively, we observe in Fig. 5 that the average torus temperature increases with  $S_\omega$ . This temperature rise is due to the increase of the Joule heating with  $S_\omega$  as well as to the limiting efficiency of the thermal plume mixing. From the DNS, we plot the horizontal average temperature of the liquid metal as a function of the vertical coordinate (Fig. 10). For RBC, the average temperature profile is antisymmetric with respect to the middle point (point reflection) and presents a sigmoid shape, with a temperature plateau equal to  $\frac{T_1+T_2}{2}$  [8]. For  $I_0 = 10$  A and  $S_\omega = 1$ , the temperature profile is close to that of RBC. When the frequency increases, the tori appear and two temperature plateaus are visible. At  $I_0 = 10$  A, the vertical temperature gradients at the top and bottom walls remains similar to RBC, indicating that the Joule effect is weak as it does not impact significantly the average heat flux on the walls. On the other hand, at  $I_0 \geq 50$  A, the temperature profiles separate from each other when the frequency varies. The differences between the curves increase with the electrical current intensity. Finally, compared to RBC, the vertical temperature gradients at the two horizontal walls are larger and grow with  $I_0$  and  $S_\omega$ . We note also that the temperature of the lower torus is systematically greater than the bottom one due to the Joule effect. Both an increase of  $Ha$  and  $S_\omega$  induce an increase of the tori average temperatures above the mean temperature  $\frac{T_1+T_2}{2}$  characteristic of RBC. All the results can be understood on the basis of dimensionless equations (5). Indeed, it is possible to evaluate the order of magnitude of the buoyancy, the Lorentz forces, and the Joule heating for the various DNSs. At  $I_0 = 10$  A and  $S_\omega = 1$ ,  $F_L \sim 1$  while  $F_B \sim 0.25$ . On the other hand, the Joule effect is negligible. The temperature profile is similar to RBC but the convection cell is broken by the Lorentz force even if the tori are not well established. At the other extremity, for  $I_0 = 100$  A and  $S_\omega = 68$ ,  $F_L \sim 8$  while  $F_B \sim 2.5 \times 10^{-3}$ . Under this condition, the Joule effect is  $2.5 \times 10^{-2}$  and is lower than the convection term of order 0.1. Hence, the Joule effect becomes significant on the temperature profiles.

The average heat flux at the bottom and top walls of the cell are calculated from the DNS. Based on the standard definition,  $Nu$  is equal to the ratio of this flux to the flux in the absence of fluid motion and Joule heating,  $Q_c$ . From Eq. (5), the difference between the bottom and top Nusselt numbers is given by

$$Nu^+ - Nu^- \sim S_\omega^{2k} Ha \sqrt{\text{Pr}_m} \Gamma. \quad (6)$$

Because our DNSs are performed in the transition regime between low and high frequencies where  $k$  changes from 1 to  $1/2$ , it is relevant to plot the heat flux as a function of the ratio  $Q_J/Q_c$  [see Fig. 3(a)]. In Fig. 11(a),  $Nu$  normalized by  $Nu_B$ , defined as the Nusselt number for RBC, is plotted as a function of  $Q_J/Q_c$ . This plot shows that the heat flux increases significantly when the Lorentz force is applied. This remarkable result can be clearly observed for the DNS at  $I_0 = 10$  A and  $S_\omega = 1$  for which  $Nu$  is increased by a factor of  $\approx 1.5$ . As long as the Joule effect can be neglected ( $Q_J/Q_c < 1$ ),  $Nu^+ \approx Nu^-$ . When the Joule heating becomes significant, at high

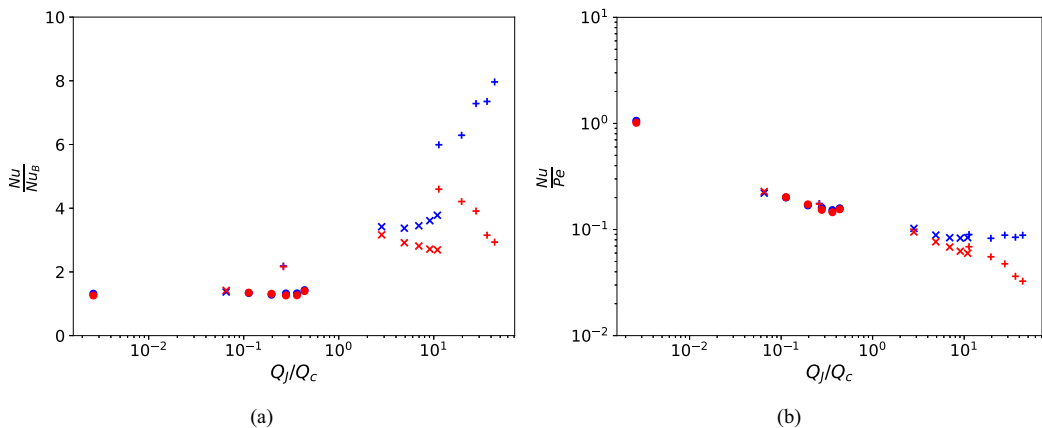


FIG. 11. Numerical results of heat flux at the top plate (blue marker) and at the bottom plate (red marker) for all values of  $I_0$  ( $\bullet = 10$  A,  $\times = 50$  A, and  $+ = 100$  A) and  $S_\omega$  (points go from left to right when  $S_\omega$  increases). The heat flux is normalized in panel (a) by the heat flux without magnetic field (RBC) and in panel (b) by the volume average convective heat flux.

frequency and current intensity, the difference between the heat flux at the bottom and the top is directly given by Eq. (6).

It is possible to obtain master curves for  $Nu^+$  and  $Nu^-$  by normalizing with the Péclet number,  $Pe = UH/\kappa$ , defined as the ratio of the convection and conduction fluxes [Fig. 11(b)]. These master curves are valid across the entire range of  $Q_J/Q_c$ . Here, the characteristic velocity  $U$  is the root-mean-square velocity of Fig. 8, which depends on frequency. Consequently,  $U \sim U_L$  at high frequency and  $U$  must be weighted by the frequency dependence of  $F_L$  at low  $S_\omega$ ,  $U \sim U_L S_\omega$ . In the intermediate-frequency regime,  $U(S_\omega)$  follows  $F_L(S_\omega)$  for a unit current intensity.

For  $Q_J/Q_c < 10^{-2}$ , corresponding to  $I_0 = 10$  A and  $S_\omega = 1$ , the Lorentz force is weak and the dynamics is intermediate between RBC and Lorentz force convection. For the other cases, we observe the same power law for  $Nu^+$  and  $Nu^-$  when  $10^{-2} \lesssim Q_J/Q_c \lesssim 1$  with an exponent of  $p \approx -1/5$ . When the Joule effect is significant ( $Q_J/Q_c > 1$ ), the  $Nu^+$  and  $Nu^-$  curves separate according to the energy balance equation (6). In the power-law regime, considering that  $Pe \sim Ha S_\omega^\alpha$  and  $Q_J \sim S_\omega^\beta Ha$  ( $\alpha = 1$  and  $\beta = 2$  at low frequency, and  $\alpha = 0$  and  $\beta = 0.5$  at high frequency), we find that  $Nu \sim Ha^{0.8} S_\omega^{0.6}$  and  $Nu \sim Ha^{0.8} S_\omega^{-0.1}$ , at low and high frequency. These relations show that  $Nu$  grows slowly when  $S_\omega$  increases at low frequency and is approximately independent of frequency when  $S_\omega > 10$ . On the other hand,  $Nu$  increases with  $Ha$ , and therefore with  $B_0$ , which increases the convection effect and the torus velocity. It is important to consider that the two scaling laws are correct in the validity range of the relationship  $Nu/Pe \sim (Q_J/Q_c)^{-1/5}$ . Finally, we observe in Fig. 11(b) that this analysis is consistent for all the DNS results.

## V. CONCLUSION

We have performed DNS for a liquid metal submitted to an ac magnetic field and a temperature gradient in a cylindrical cell. We have studied the dynamics of the liquid metal for  $30 \leq Ha \leq 301$  and  $1 \leq S_\omega \leq 68$ . The local Lorentz force and the Joule heating scale in  $S_\omega^k$  and  $S_\omega^{2k}$ , respectively, where  $k = 1$  at low frequency and  $k = 1/2$  at high frequency. The interest of this study is that the DNSs are realized in the intermediate regimes between low and high frequency and for different  $Ha$ , a situation that is encountered in various applications.

Under our DNS conditions, the appropriate scale of temperature is the temperature difference  $\Delta T_0$  and the velocity scale is given by the Alfvén velocity  $U_L$ . Hence, the DNSs are realized under

conditions where the Lorentz force dominates the buoyancy force and the Joule heating has a lower impact on fluid flow.

We observed from the temperature and flow patterns issued from the simulations that the Lorentz force, even at low magnitude, changes drastically the RBC structure of the flow and imposes a two-tori pattern. We established that the fluid velocity increases with  $Ha$  and with  $S_\omega$  at low frequency and decreases slowly for  $S_\omega > 10$  until it reaches a constant limit. Compared to RBC, the temperature is significantly altered by the tori: each torus is characterized by a different average temperature, which leads to different temperature gradients at the bottom and the top walls and, consequently, to different heat transfer to the outside. The simulations show clearly that the average temperature increases with the Joule heating.

This study points out that  $F_L$  enhances the heat transfer even at a low  $Ha$  number. All the data merge in a master curve when  $Nu/Pe$  is plotted vs  $Q_J/Q_c$  which exhibits a power-law regime for intermediate values of  $Q_J/Q_c$ ,  $Nu/Pe \sim (Q_J/Q_c)^p$  with  $p \approx -1/5$ . We have established the scaling law between  $Nu$ ,  $Ha$ , and  $S_\omega$  at low- and high-frequency regimes and in the case where the Joule effect is moderate. Under these conditions, the Nusselt number follows the scaling law:  $Nu \sim Ha^{0.8} S_\omega^{0.6}$  and  $Nu \sim Ha^{0.8} S_\omega^{-0.1}$ , respectively.

These DNSs in this range of physical parameters applied in industrial applications show the importance of the Lorentz force on the dynamics and on the heat transfer even under conditions where the temperature gradients are large. In addition, it is possible to counterbalance the buoyancy force by the Lorentz force produced by a moderate ac magnetic field.

#### ACKNOWLEDGMENTS

Our DNS simulations were performed using high-performance computing resources from GENCI-CINES and GENCI-IDRIS (Grant No. A0112B07400) and the CALMIP Centre of the University of Toulouse (Grant No. P0910). The authors acknowledge the French Nuclear Energy Center (CEA) in Cadarache for its financial support. They thank also Yvan Lefevre for fruitful discussions.

#### APPENDIX: EFFECT OF THE MAGNETIC FIELD PERTURBATION

We consider a liquid metal moving in an ac magnetic field. The time and spatial distribution of the magnetic field  $\mathbf{B}(\mathbf{r}, t)$  is given by the induction equation:

$$\frac{\partial \mathbf{B}}{\partial t} = \nabla \times (\mathbf{u} \times \mathbf{B}) + \frac{1}{\eta} \Delta \mathbf{B}, \quad (\text{A1})$$

where  $\mathbf{u}$  is the liquid velocity and  $\eta$  is the magnetic diffusion. The magnetic field can be decomposed in two terms:

$$\mathbf{B} = \mathbf{B}_0 + \mathbf{b}, \quad (\text{A2})$$

where  $\mathbf{B}_0(\mathbf{r}, t)$  is the magnetic field when the fluid is at rest, and  $\mathbf{b}(\mathbf{r}, t)$  is the magnetic field perturbation due to the induction by the motion of the liquid.

In consequence, the resulting eddy currents  $\mathbf{J}(\mathbf{r}, t)$  in the liquid can be decomposed in two terms:

$$\mathbf{J} = \mathbf{J}_0 + \mathbf{j}, \quad (\text{A3})$$

where

$$\mathbf{J}_0 = \sigma \mathbf{E}_0 \quad \text{and} \quad \mathbf{j} = \sigma (\mathbf{e} + \mathbf{u} \times \mathbf{B}_0 + \mathbf{u} \times \mathbf{b}). \quad (\text{A4})$$

Here  $\mathbf{E}_0$  is the electrical field related to  $\mathbf{B}_0$  by the Maxwell-Faraday equation,  $\mathbf{e}$  is the electric field perturbation, and  $\sigma$  is the electrical conductivity of the liquid.

The Lorentz force  $\mathbf{F}_L$  can be decomposed in four terms:

$$\mathbf{F}_L = \mathbf{J}_0 \times \mathbf{B}_0 + \mathbf{j} \times \mathbf{B}_0 + \mathbf{j} \times \mathbf{b} + \mathbf{J}_0 \times \mathbf{b}. \quad (\text{A5})$$

The Reynolds magnetic number  $\text{Re}_m$  is defined as the ratio of the magnetic convection and the diffusion effects in Eq. (A1). Assuming that  $\text{Re}_m \ll 1$ ,  $b \approx \text{Re}_m \mathbf{B}_0$ ,  $\mathbf{J}_0 \times \mathbf{B}_0 \gg \mathbf{J}_0 \times \mathbf{b}$  and  $\mathbf{j} \times \mathbf{B}_0 \gg \mathbf{j} \times \mathbf{b}$ . Under these conditions, the intensity of the Lorentz force can be approximated by

$$F_L \approx \sigma E_0 B_0 + \sigma (e + u B_0) B_0. \quad (\text{A6})$$

At high frequency, according to the Maxwell-Faraday equation,  $E_0 \sim \omega \delta B_0$  and  $e \sim \omega \delta b$ , where  $\delta = \sqrt{2\eta/\omega}$  is the skin depth of the magnetic field. Note that  $E_0 \gg e$ . In consequence, the Lorentz force becomes

$$F_L \approx \sigma \omega \delta B_0^2 + \sigma u B_0^2. \quad (\text{A7})$$

The ratio of the two terms on the right-hand side of Eq. (A7) is  $\frac{\sqrt{2S_\omega}}{\text{Re}_m}$ , where  $S_\omega = 2L^2/\delta^2$  is the shielding parameter ( $L$  is the characteristic length of the liquid flow).

In conclusion, when  $\text{Re}_m \ll 1$  and  $\frac{\sqrt{2S_\omega}}{\text{Re}_m} \gg 1$ , the perturbation of the magnetic field can be neglected and the Lorentz force can be approximated by  $\sigma \omega \delta B_0^2$ .

- 
- [1] R. Moreau, *Magnetohydrodynamics* (Springer Science & Business Media, Dordrecht, 1990).
  - [2] P. A. Davidson, *An Introduction to Magnetohydrodynamics* (Cambridge University Press, Cambridge, 2001).
  - [3] V. Bojarevics and A. Tucs, MHD of large scale liquid metal batteries, in *Light Metals 2017* (Springer, Berlin, 2017), pp. 687–692.
  - [4] C. Journeau, P. Piluso, J.-F. Haquet, E. Boccaccio, V. Saldo, J.-M. Bonnet, S. Malaval, L. Carénini, and L. Brissonneau, Two-dimensional interaction of oxidic corium with concretes: The VULCANO VB test series, *Ann. Nucl. Energy* **36**, 1597 (2009).
  - [5] S. Grossmann and D. Lohse, Scaling in thermal convection: a unifying theory, *J. Fluid Mech.* **407**, 27 (2000).
  - [6] P. Frick, R. Khalilov, I. Kolesnichenko, A. Mamykin, V. Pakholkov, A. Pavlinov, and S. Rogozhkin, Turbulent convective heat transfer in a long cylinder with liquid sodium, *Europhys. Lett.* **109**, 14002 (2015).
  - [7] F. Chilla, M. Rastello, S. Chaumat, and B. Castaing, Long relaxation times and tilt sensitivity in Rayleigh-Bénard turbulence, *Eur. Phys. J. B* **40**, 223 (2004).
  - [8] D. Goluskin, *Internally Heated Convection and Rayleigh-Bénard Convection* (Springer, Berlin, 2016).
  - [9] D. Goluskin and E. P. van der Poel, Penetrative internally heated convection in two and three dimensions, *J. Fluid Mech.* **791**, R6 (2016).
  - [10] D. J. Tritton and M. N. Zarraga, Convection in horizontal layers with internal heat generation: Experiments, *J. Fluid Mech.* **30**, 21 (1967).
  - [11] L. Xiang and O. Zikanov, Subcritical convection in an internally heated layer, *Phys. Rev. Fluids* **2**, 063501 (2017).
  - [12] B.-F. Wang, L. Zhou, Z.-H. Wan, D.-J. Ma, and D.-J. Sun, Stability analysis of Rayleigh-Bénard convection in a cylinder with internal heat generation, *Phys. Rev. E* **94**, 013108 (2016).
  - [13] H. K. Moffatt, Electromagnetic stirring, *Phys. Fluids A* **3**, 1336 (1991).
  - [14] E. Taberlet and Y. Fautrelle, Turbulent stirring in an experimental induction furnace, *J. Fluid Mech.* **159**, 409 (1985).
  - [15] B. Knaepen, S. Kassinos, and D. Carati, Magnetohydrodynamic turbulence at moderate magnetic Reynolds number, *J. Fluid Mech.* **513**, 199 (1999).
  - [16] T. Zürner, W. Liu, D. Krasnov, and J. Schumacher, Heat and momentum transfer for magnetoconvection in a vertical external magnetic field, *Phys. Rev. E* **94**, 043108 (2016).
  - [17] R. Akhmedagaev, O. Zikanov, D. Krasnov, and J. Schumacher, Turbulent Rayleigh-Bénard convection in a strong vertical magnetic field, *J. Fluid Mech.* **895**, R4 (2020).

- [18] S. R. de Vaux, R. Zamansky, W. Bergez, P. Tordjeman, and J.-F. Haquet, Magnetoconvection transient dynamics by numerical simulation, *Eur. Phys. J. E* **40**, 13 (2017).
- [19] S. Renaudière de Vaux, R. Zamansky, W. Bergez, P. Tordjeman, and J.-F. Haquet, Destabilization of a liquid metal by nonuniform Joule heating, *Phys. Rev. E* **96**, 033103 (2017).
- [20] I. L. Nikulin and A. V. Perminov, Mathematical modelling of frequency and force impacts on averaged metal flows in alternating magnetic field, *Int. J. Heat Mass Transfer* **128**, 1026 (2019).
- [21] G. S. Charlson and R. L. Sani, Thermoconvective instability in a bounded cylindrical fluid layer, *Int. J. Heat Mass Transfer* **13**, 1479 (1970).
- [22] J. Magnaudet, M. Rivero, and J. Fabre, Accelerated flows past a rigid sphere or a spherical bubble. Part 1. Steady straining flow, *J. Fluid Mech.* **284**, 97 (1995).
- [23] G. Grötzbach, Spatial resolution requirements for direct numerical simulation of the Rayleigh-Bénard convection, *J. Comput. Phys.* **49**, 241 (1983).
- [24] See Supplemental Material at <http://link.aps.org/supplemental/10.1103/PhysRevFluids.7.073701> for numerical methods and DNS videos.
- [25] S. Cioni, S. Ciliberto, and J. Sommeria, Strongly turbulent Rayleigh-Bénard convection in mercury: comparison with results at moderate Prandtl number, *J. Fluid Mech.* **335**, 111 (1997).
- [26] T. Zürner, F. Schindler, T. Vogt, S. Eckert, and J. Schumacher, Combined measurement of velocity and temperature in liquid metal convection, *J. Fluid Mech.* **876**, 1108 (2019).